International Journal for Multiscale Computational Engineering, 5(6)447–459(2007)

Studies of Nanotube-Based Aluminum Composites Using the Bridging Domain Coupling Method

Shaoping Xiao & Wenyi Hou

Department of Mechanical and Industrial Engineering, Center for Computer-Aided Design, University of Iowa, Iowa City, IA 52242, USA

ABSTRACT

In this article, after performing verification of the bridging domain coupling method in a three-dimensional application, we employ this coupling method to study Young's moduli and failure strengths of nanotube-based aluminum composites. In the multiscale model of nanocomposites, the nanotubes and their surrounding areas, i.e., the interaction zones, are modeled via molecular dynamics, while the other regions are modeled via the finite element method. Three types of nanotubes are considered as inclusions: single-walled carbon nanotubes (SWNTs), multiwalled carbon nanotubes (MWNTs), and SWNT bundles. Although all types of nanotube inclusions can reinforce nanocomposites, MWNTs play the most significant role compared to the other two inclusions. In addition, SWNT bundles are better inclusions than SWNTs for reinforcing nanocomposites.

KEYWORDS

carbon nanotubes, composites, bridging domain, multiscale, fracture

*Address all correspondence to shaoping-xiao@uiowa.edu

1. INTRODUCTION

The discovery of carbon nanotubes (CNTs) in 1991 [1] inspired the researchers to intensively study mechanics of CNTs and their applications in nanoscale materials and devices [2,3]. CNTs have large interfacial area per volume and possess large tensile moduli and high thermal conductivities [4,5]. The Young's moduli of CNTs were predicted to be up to 1 TPa; their thermal conductivities could be as high as 6600 W/m K. Therefore they have been proposed as ideal fibers for manufacturing the next generation of composite materials with mechanical and thermal management applications [6,7]. Dalton et al. [6] obtained exceptionally strong CNT fibers that were tougher than spider silk or any fiber used for mechanical reinforcement. Due to volume expansion and polar interaction of various vapors on the CNT surface, [7] found that there was an increase in resistance of the order of 100–1000 when CNT-polymethylmethacrylate composite thin films were exposed to dichloromethane, chloroform, and acetone.

Generally, three types of materials were employed as the matrix in CNT-embedded composites: polymers [7,8], ceramics [9], and metals [10]. Since polymers have low density and are easy to shape, they are the first choice for the matrix of CNT-reinforced composites. Due to the properties of light weight and high stiffness/strength, CNT-polymer composites have emerged in the materials science field as promising materials for aerospace, naval, automobile, and other civil and industrial applications. As structural materials, ceramics present many advantages over polymers, such as high rigidity and hardness, even at high temperatures, and low sensitivity to corrosion. However, they are brittle. Reinforcing the ceramic composites with CNTs can make up such a weakness. Recently, there has been interest in using metal composites to competitive advantage to provide weight or performance benefits. Kuzumaki and coworkers [11] produced a CNT-aluminum nanocomposite wire and found that this wire could retain its strength at as high as 1000 K, at which the strength of pure aluminum could decrease by 50%.

The key to studying nanotube-embedded nanocomposites is to understand the mechanism of interfacial interaction, i.e., load transfer, between nanotubes and the matrix material because the efficiency of interfacial load transfer determines the reinforcement of nanocomposites via embedding nanotubes into the matrix material. The interfacial load transfer can have the following situations: (1) weak load transfer due to nonbonded interaction between the matrix and CNTs [11]; (2) a strong nonbonded interaction between the matrix (polymer) and CNTs by wrapping polymer chains around CNTs [12]; and (3) strong load transfer due to the functionalization approach, involving the formation of chemical covalent bonds between CNTs and the matrix [13]. Molecular dynamics (MD) is a powerful tool for revealing complex physical phenomena, including a load transfer mechanism at the CNT-matrix interface [14,15]. Xiao and Hou [15] conducted a molecular dynamics simulation to study the mechanical properties and fracture of nanotube-based aluminum composites. They pointed out that the fracture toughness of metal matrix composites with nanotubes could be increased by up to 200%. However, MD exhibits severe limitations with respect to both length and time scales. The models studied by Xiao and Hou [15] contained only a total of 1000 atoms, so detailed fracture behavior of nanocomposites could not be investigated. The recently developed multiscale methods can provide an alternative solution.

Multiscale methods can be divided into two classes: hierarchical multiscale methods [16,17] and concurrent multiscale methods [18,19]. In most hierarchical modeling, the continuum approximation is based on the properties of a subscale model, such as an MD model. The intrinsic properties of the material are determined at the atomic level and embedded in the continuum model according to a homogenization procedure [20,21]. Concurrent multiscale methods employ an appropriate coupling model, usually atomistic/continuum coupling, in different subdomains to treat each length scale simultaneously. One of the first atomistic/continuum coupling methods was macroscopic atomistic ab initio dynamics [22]. This method coupled the molecular dynamics model with the continuum model via a "handshake" domain, in which the two Hamiltonians were averaged. To reduce spurious reflections into the molecular dynamics domain, damping could be used in the handshake region, although the damping was not based on any rigorous theory. In most cases, it appears that the finite element continuum model had to be nearly of the scale of inter-

atomic distances at the atomistic-continuum interface to perform well. Consequently, a unique molecular dynamics time step was used in the whole multiscale model. To overcome the above issues, [23,24] developed the bridging scale multiscale method, in which MD was used only in a localized region, while the continuum simulation covered the entire domain, including the MD region to which it was coupled. The bridging domain coupling method developed by [25,26] can also avoid spurious wave reflection without any additional filtering or damping. In addition, since uniform meshes were utilized in the continuum model, a large time step is utilized in the continuum model, while a small time step is utilized in the molecular model. Recently, [27] mathematically demonstrated that the bridging domain coupling was stable.

Researchers have used multiscale concepts to model and simulate nanocomposites. Xia and Curtin [28] proposed a three-dimensional finite element approach to failure of composite materials. They employed the knowledge of micromechanics to study load transfer between nanofibers and the aluminum matrix. Namilae and Chandra [29] developed a hierarchical multiscale methodology linking MD and the finite element method through atomically informed cohesive zone model parameters to represent the CNT-matrix interfaces. However, using the continuum approach, such as micromechanics or the cohesive zone model, instead of direct MD simulation may not precisely describe the CNT-matrix interfacial interactions. In this article, we plan to generate an atomistic/continuum multiscale model for nanotube-based composites using the bridging domain coupling method [25,26]. The molecular domain should include the nanotubes and their surrounding areas, i.e., the interaction zones, while the other regions of nanocomposites are modeled via the continuum approximation such as the finite element method. We choose aluminum as the matrix material because crystalline solids are easy to model via the atomistic/continuum coupling method. Obviously, such a multiscale model can be extended to study other nanocomposites, including polymer composites.

The outline of this article is as follows. In Section 2, we briefly introduce the bridging domain coupling method. We present a three-dimensional verification in Section 3. In the fourth section, the bridging domain coupling method is employed to study Young's moduli of nanotube-based aluminum composites. We consider single-walled carbon nanotubes (SWNTs), multiwalled carbon nanotubes (MWNTs), and SWNT bundles as inclusions. In Section 5, we investigate the fracture of nanocomposites, and conclusions are presented in Section 6.

2. BRIDGING DOMAIN COUPLING METHOD

In the bridging domain coupling method [25,26], the molecular domain Ω_0^M and the continuum domain Ω_0^C are overlapped through the bridging domain Ω_0^{int}, i.e., the overlapping subdomain, as shown in Fig. 1. A scaling parameter α is introduced in the bridging domain and is defined as

$$\alpha = \begin{cases} 1 & \text{in} \quad \Omega_0^C - \Omega_0^{\text{int}} \\ [0,1] & \text{in} \quad \Omega_0^{\text{int}} \\ 0 & \text{in} \quad \Omega_0^M - \Omega_0^{\text{int}} \end{cases} \tag{1}$$

Indeed, α is a function of coordinates that vanishes in the molecular domain, equals unity in the continuum domain, and increases smoothly from 0 to 1 in the bridging domain. It should be noted that α was easily constructed as a linear function for a bridging domain with regular shape. If a bridging domain has irregular shape, the radial basis function can be employed to define α, which can be a nonlinear function. In this article, molecular mechanics/dynamics is employed in the molecular domain, while the finite element method is employed in the continuum domain. The two domains are constrained on the bridging domain via

$$\mathbf{g}_I = \{g_{iI}\} = \{u_i(\mathbf{X}_I) - d_{iI}\} = \left\{\sum_J N_{JI} u_{iJ} - d_{iI}\right\} = 0 \tag{2}$$

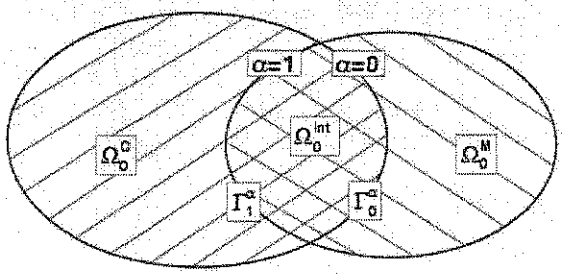

FIGURE 1. A scheme of the bridging domain coupling method

The atomic displacements $\mathbf{d}$ are required to conform to the continuum displacements $\mathbf{u}$ at the positions of the atoms in the bridging domain. $N_{JI} = N_J(\mathbf{X}_I)$ are finite element interpolation functions or shape functions. The constraints are applied to all components of the displacements.

Using the Lagrange multiplier method, the total energy of the complete domain can be written as a linear combination of the molecular and continuum energies:

$$W_L(\mathbf{x}) = (1-\alpha) W^M(\mathbf{x}) + \int_{\Omega_0^C} \alpha w^C d\Omega_0^C + \sum_I \lambda_I^T \mathbf{g}_I \quad (3)$$

where $W^M(\mathbf{x})$ is the potential function, which is the sum of the energies due to any force fields, such as pairwise interaction of the atoms, three-body potentials, or others. Term $w^C(\mathbf{x})$ is the strain energy density in the continuum domain. The strain energy density can be calculated from molecular potential through a homogenization technique. It should be noted that if temperature effects need to be considered, the temperature-related homogenization technique [20,21] must be employed. In this case, the strain energy density should be replaced by the free energy density in Eq. (3). Term $\boldsymbol{\lambda}_I = \{\lambda_{iI}\}$ is a vector of Lagrange multipliers whose components correspond to the components of the displacement of atom I in the bridging domain.

In a quasi-static problem, minimization of the system energy is conducted under any given boundary condition. In this case, the unknowns of the above multiscale model include atomic displacements, finite element nodal displacements, and Lagrange multipliers. Therefore the problem becomes solving the following discrete equations, usually using the conjugated gradient method:

$$\frac{\partial W_L}{\partial \mathbf{u}} = 0, \quad \frac{\partial W_L}{\partial \mathbf{d}} = 0, \quad \frac{\partial W_L}{\partial \boldsymbol{\lambda}} = 0 \quad (4)$$

To study the time-dependent physical phenomena of a nanosystem, the Hamiltonian should be considered. Similar to Eq. (3), the total Hamiltonian is a linear combination of the molecular and continuum Hamiltonians, i.e., H^M and H^C, and it is written as follows:

$$\begin{aligned} H_L &= (1-\alpha) H^M + \alpha H^C + \sum_I \boldsymbol{\lambda}_I^T \mathbf{g}_I \\ &= \sum_J (1-\alpha_J) \frac{\mathbf{p}_J^M \cdot \mathbf{p}_J^M}{2m_J} + (1-\alpha) W^M \\ &\quad + \sum_K \alpha_K \frac{\mathbf{p}_K^C \cdot \mathbf{p}_K^C}{2M_K} + \int \alpha w^C d\Omega_0^C + \sum_I \boldsymbol{\lambda}_I^T \mathbf{g}_I \quad (5) \end{aligned}$$

where $\mathbf{p}_J^M$ is the momentum of atom J with the mass m_J, and $\mathbf{p}_K^C$ is the momentum of finite element node K with the mass M_K. Then, the equations of motion are derived as

$$\bar{M}_K \ddot{\mathbf{u}}_K = \mathbf{F}_K^{\text{ext}} - \mathbf{F}_K^{\text{int}} - \mathbf{F}_K^L \text{ in } \Omega_0^C \quad (6)$$

$$\bar{m}_J \ddot{\mathbf{d}}_J = \mathbf{f}_J^{\text{ext}} - \frac{\partial W^M}{\partial \mathbf{d}_J} - \mathbf{f}_J^L \text{ in } \Omega_0^M \quad (7)$$

where $\bar{M}_K = \alpha_K M_K$ and $\bar{m}_J = (1-\alpha_J) m_J$. $\mathbf{F}_K^{\text{ext}}$ and $\mathbf{F}_K^{int}$ are nodal external and internal forces in the finite element continuum domain, and they can be calculated using the conventional nonlinear finite element method [30]; $\mathbf{f}_J^{\text{ext}}$ are external forces, such as electrostatic forces, applied on atoms. $\mathbf{F}_K^L$ and $\mathbf{f}_J^L$ are forces on nodes and atoms, respectively, in the bridging domain due to constraints. They are calculated as

$$\mathbf{F}_K^L = \sum_I \boldsymbol{\lambda}_I^T \frac{\partial \mathbf{g}_I}{\partial \mathbf{u}_K} = \sum_I \boldsymbol{\lambda}_I^T [N_{IK} \mathbf{I}] \quad (8)$$

$$\mathbf{f}_J^L = \sum_I \boldsymbol{\lambda}_I^T \frac{\partial \mathbf{g}_I}{\partial \mathbf{d}_J} = -\sum_I \boldsymbol{\lambda}_I^T [\delta_{IJ} \mathbf{I}] \quad (9)$$

An explicit algorithm for updating motions of atoms and nodes during multiscale simulations has been developed by [24]. At first, so-called trial velocities are obtained independently in the continuum and molecular domains via solving Eqs. (6) and (7) without considering constraint forces $\mathbf{F}_K^L$ and $\mathbf{f}_J^L$. Then, the time derivatives of constraints, Eq. (2), are applied to calculate the Lagrange multipliers. Finally, the constraint forces calculated from Eqs. (8) and (9) are substituted back to Eqs. (6) and (7) to correct the trial nodal/atomic velocities in the bridging domain. The developed bridging domain coupling method can automatically eliminate wave reflection, a nonphysical phenomenon due to the length scale variation, as detailed by [26].

3. VERIFICATION OF MULTISCALE METHOD

Belytschko and Xiao [25] and Xiao and Belytschko [26] studied one- and two-dimensional examples to verify the bridging domain coupling method. In this article, we perform a three-dimensional verification. We investigate a bar of aluminum (Al) subject to uniaxial tension or compression via the bridging domain coupling method and compare the calculated stress-strain relation with the one from MD simulation. The simulated Al crystalline bar has the following dimensions: length of 5.6 nm, width of 1.6 nm, and height of 1.6 nm, and it has 1013 Al atoms. Fig. 2 illustrates the molecular model and the bridging domain coupling model of this Al crystalline bar. Since the bridging domain here has the regular shape of a block, shown in Fig. 2(b), α is a linear function along the axial direction of the Al crystalline bar. In this multiscale model, the tetrahedral elements are generated in the continuum domain. Consequently, there are 689 Al atoms and 65 finite element nodes in Fig. 2(b).

We use the following embedded atom method (EAM). potential function [31,32] to describe the interatomic interaction in the Al crystalline:

$$E_{\mathrm{Al}} = \frac{1}{2}\sum_{ij} V(r_{ij}) + \sum_{i} F(\bar{\rho}_i) \tag{10}$$

where $V(r_{ij})$ is a pairwise potential as a function of distance between atom i and atom j, and F is the "embedding energy" as a function of the "atomic density" $\bar{\rho}_i$ that represents the environment effects of all surrounding atoms in the system. The latter is given by

$$\bar{\rho}_i = \sum_{j \neq i} \rho(r_{ij}) \tag{11}$$

where $\rho(r_{ij})$ is the "atomic density" function.

In molecular dynamics simulations, the following equations of motion are solved for the whole simulated system without the consideration of external forces:

$$m_I \ddot{\mathbf{d}}_I = -\frac{\partial E_{AL}}{\partial \mathbf{x}_I} \tag{12}$$

where m_I is the mass of atom I, $\mathbf{x}_I$ is its position, and $\mathbf{x}_I = \mathbf{X}_I + \mathbf{d}_I$ ($\mathbf{X}_I$ is the original position of atom I and $\mathbf{d}_I$ is its displacement). A Hoover thermostat [33] is implemented so a constant temperature can be maintained during MD simulations. In this article, all the simulations are subject to the room temperature of 300 K. To investigate the stress-strain relation of the Al crystalline bar under uniaxial tension or compression, one end of the bar is fixed, and the other end is applied via the prescribed displacement with the increment or decrement of 1.0×10^{-6} nm/fs during the simulation. For each displacement increment/decrement, the Al crystalline bar is equilibrated for 1000 time steps. Another 100 time steps are used to calculate the time-averaged external force F. The external force F, which corresponds to the prescribed displacement, can be calculated by summing the internal forces of the atoms with the prescribed displacement. One can obtain the stress via $\sigma = F/A$, where $A = 2.56$ nm^2 is the cross-sectional area of the Al crystalline bar.

In the bridging domain coupling simulation, the end of the bar in the continuum model is fixed,

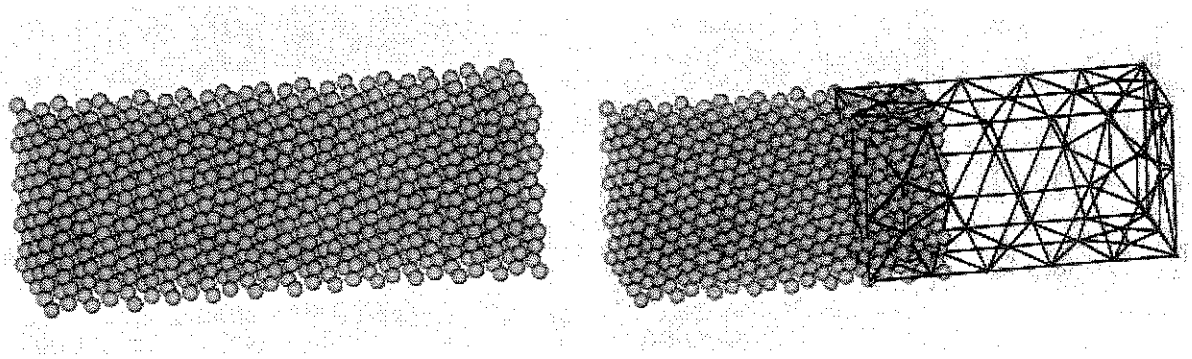

(a) (b)

FIGURE 2. Numerical models of an aluminum crystalline bar: **a)** molecular model; **b)** bridging domain coupling model

and the other end in the molecular model is applied with the same prescribed displacement as described above. In the continuum domain, linear elasticity is assumed so that material properties are derived from the subscale (the molecular scale), instead of implementing the homogenization technique to simplify the problem. To derive the material properties, we employ the representative volume element (RVE) technique with MD simulation and obtain the following material properties at the room temperature of 300 K: Young's modulus of 78.02 GPa and Poisson's ratio of 0.325.

The comparison of calculated stress-strain relations between MD simulation and multiscale simulation at the room temperature of 300 K is illustrated in Fig. 3. The stress-strain relations are almost linear, and we can see that they are in good agreement.

4. YOUNG'S MODULI OF CARBON NANOTUBE (CNT)-ALUMINUM COMPOSITES

In this section, we employ the bridging domain coupling method to study material properties, especially Young's moduli, of CNT-reinforced Al composites. It should be noted that we only consider pristine nanotubes since a defected tube plays a different role when embedding in composites; see details provided by [15]. We first consider SWNTs and assume that long SWNTs are aligned unidirectionally and distributed homogeneously in the Al matrix. Therefore we use a unit cell model, shown in Fig. 4, with periodic boundary conditions to investigate Young's moduli of nanocomposites.

The cell model in Fig. 4 contains an SWNT. In the coupling model, the SWNT is embedded in the center of the unit cell. The bridging domain is a circular band with the outer radius of r_o and the inner radius of r_i between the molecular and continuum domains. Therefore the scaling parameter α is defined as a linear function of $(r - r_i)/(r_o - r_i)$, where r is the distance of the projection to the tube axis, as shown in Fig. 5. Except in the bridging do-

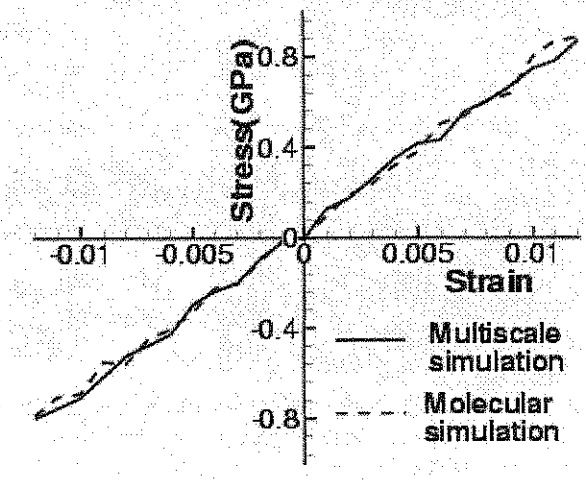

FIGURE 3. Comparison of stress-strain relations at room temperature

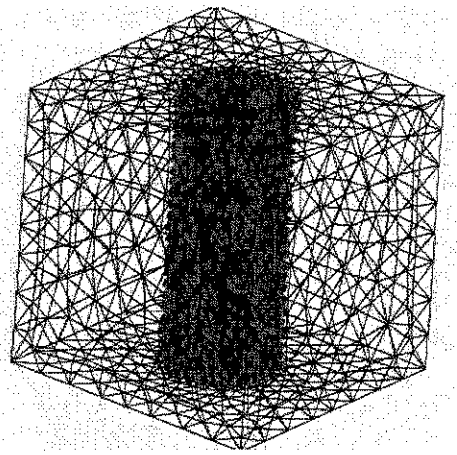

(a)

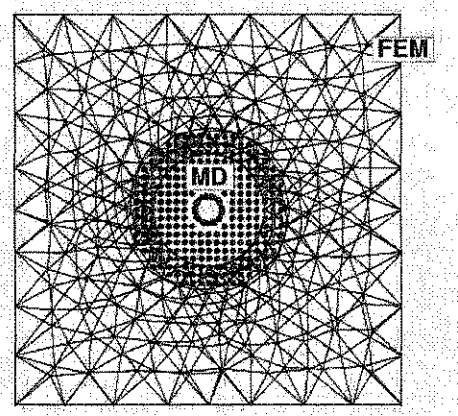

(b)

FIGURE 4. Bridging domain coupling model of SWNT/Al nanocomposites: **(a)** three-dimensional view; **(b)** top view

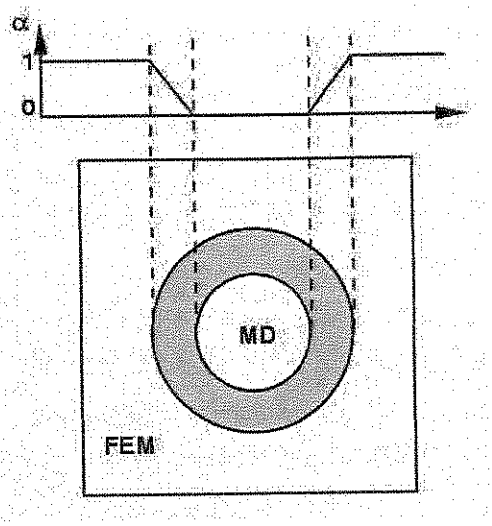

FIGURE 5. Scaling parameter in the multiscale model of nanocomposites

main, α is 0 in the molecular domain and 1 in the continuum domain. Obviously, α is an axially symmetric function.

We employ the finite element method with tetrahedral elements in the continuum model. The material properties at the room temperature of 300 K are Young's modulus of 78.02 GPa and Poisson's ratio of 0.325. In the molecular model, molecular dynamics with the Hoover thermostat is used. We use the modified Morse potential function [34] to describe interatomic interaction between bonded carbon atoms in SWNT. This potential can be written as

$$E = E_{\text{stretch}} + E_{\text{angle}}$$

$$E_{\text{stretch}} = D_e \left\{ \left[1 - e^{-\beta(r-r_0)} \right]^2 - 1 \right\} \qquad (13)$$

$$E_{\text{angle}} = \frac{1}{2} k_\theta \left(\theta - \theta_0 \right)^2 \left[1 + k_s \left(\theta - \theta_0 \right)^4 \right]$$

where E_{stretch} is the bond energy due to bond stretching or compressing, E_{angle} is the bond energy due to bond angle bending, r is the current bond length, and θ is the angle of two adjacent bonds representing a standard deformation measure in molecular mechanics. The parameters are

$$r_0 = 1.42 \times 10^{-10} \text{ m}, \; D_e = 6.03105 \times 10^{-19} \text{ Nm}$$

$$r_0 = 1.42 \times 10^{-10} \text{ m}, \; \theta_0 = 2.094 \text{ rad} \qquad (14)$$

$$k_\theta = 1.13 \times 10^{-18} \text{ Nm/rad}^2, \; k_s = 0.754 \text{ rad}^{-4}$$

Since only weak CNT-Al interfaces were observed in the experimentation [11], the Lennard-Jones potential, as follows, is used to describe nonbonded interaction between the embedded carbon nanotube and the aluminum matrix:

$$E_{LJ} = 4\varepsilon \left[\left(\frac{\sigma}{r} \right)^{12} - \left(\frac{\sigma}{r} \right)^{6} \right] \qquad (15)$$

The parameters for the interactions between carbon atoms and Al atoms are obtained from the Lorentz-Berelot combining rules: $\varepsilon = 0.038$ eV and $\sigma = 0.296$ nm.

To calculate Young's moduli of nanocomposites, we investigate the stress-strain relations of nanocomposites first. The prescribed displacement is applied on the top of the unit cell, while the bottom of the unit cell is fixed. Since the long tube is considered and the periodic boundary condition is employed, the prescribed displacement is applied on both the nanotube and the Al matrix. We evaluate stress at every 0.1% strain during the simulation via summing the internal forces on the nodes/atoms on the top of the unit cell and then dividing it by the cross-sectional area of the cell. The Young's modulus is then calculated as the slope of the stress-strain relation curve. In this section, we mainly investigate Young's moduli of nanocomposites with various volume fractions of embedded CNTs at the room temperature of 300 K.

We consider two SWNTs, respectively, as inclusions in the Al matrix material. One is the (5,5) SWNT with a diameter of 0.68 nm, while the other is the (21,21) SWNT with a diameter of 2.85 nm. We vary the size of the unit cell so that various volume fractions of embedded tubes can be achieved. Table 1 illustrates the calculated Young's moduli of nanocomposites with various tube volume fractions at the room temperature. Apparently, a larger volume fraction of embedded SWNTs results in a larger Young's modulus of nanocomposites. It also can be seen that the Young's moduli of nanocomposites are similar, no matter which SWNTs are embedded, for a given tube volume fraction. In other words, nanotube size has no effect on

TABLE 1. Young's moduli of SWNT-based Al nanocomposites with various tube volume fractions at room temperature

	SWNT volume fraction (%)					
Young's moduli of nanocomposites, GPa	1.3	1.8	4.1	7.3	11.4	16.4
With (5,5) SWNTs	85.0	86.8	89.4	96.6	101.4	118.0
With (21,21) SWNTs	84.2	86.4	90.1	97.7	103.2	115.7

the Young's modulus of nanocomposites. This is because size effects on nanotubes' stiffness are significant only for nanotubes with small diameters [35]. Therefore there is no effect of tube size on Young's moduli of nanotube-reinforced composites.

As utilized in the experiments [36], most fabricated CNTs are multiwalled nanotubes (MWNTs) or SWNT bundles. An MWNT contains a number of coaxial SWNTs, and the interlayer distance between SWNTs is 0.34 nm. In SWNT bundles, SWNTs are packed in two-dimensional triangular lattices. The nearest distance between two neighboring SWNTs is also 0.34 nm. The Lennard-Jones potential [37], similar to Eq. (15), is employed to describe nonbonded interaction between two carbon atoms that are located at different SWNTs in MWNTs or SWNT bundles. The parameters are $\varepsilon = 0.0025$ eV and $\sigma = 0.34$ nm.

In our multiscale simulations, we select a (21,21) MWNT, which contains (21,21), (16,16), (11,11), and (6,6) SWNTs, and a (5,5) SWNT bundle, which contains seven (5,5) SWNTs. The multiscale models are illustrated in Figs. 6(a) and 6(b), respectively. The scaling parameters in the bridging domains can be constructed similarly to the one in Fig. 5. It should be noted that all the (21,21) SWNT, (21,21) MWNT, and (5,5) SWNT bundles have similar diameters. Fig. 7 compares the roles of the above three nanotube inclusions in reinforcement of nanocomposites. It is evident that the MWNT results in the most significant reinforcement, followed by the SWNT bundle. The SWNT results in the least significant reinforcement compared to the other two inclusions. As an instance of 10% CNT volume fraction, the nanocomposite containing (21,21) SWNTs has the Young's modulus of 100 GPa. However, the nanocomposite containing (5,5) SWNT bundles can have the Young's modulus of 110 GPa, and the one containing (21,21) MWNTs can have the Young's modulus of as high as 135 GPa.

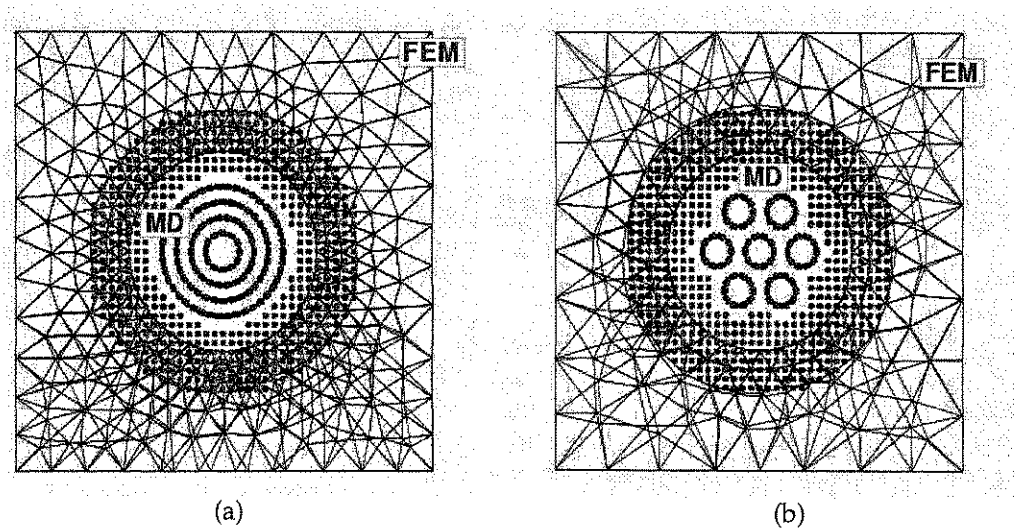

FIGURE 6. Multiscale models of nanocomposites (top views): **a)** nanocomposite with an MWNT; **b)** nanocomposite with an SWNT bundle

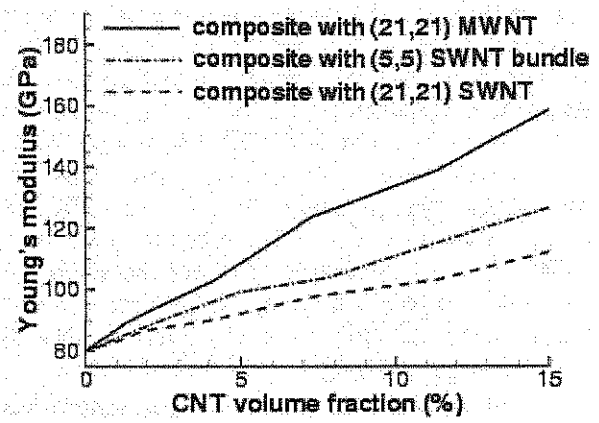

FIGURE 7. Young's moduli of nanocomposites at various CNT volume fractions

5. FRACTURE OF CNT-ALUMINUM COMPOSITES

Using the bridging domain coupling method, we also investigate the crack propagation inside Al composites embedded with CNTs. An example is provided in Fig. 8: The entire composite model contains a molecular domain, including a (5,5) SWNT and its surrounding region (interaction zone), two finite element domains, and two bridging domains. Tetrahedral elements are selected to discretize the continuum domains. There are 660 carbon atoms and 12,316 Al atoms in the molecular domain and 467 finite element nodes in the continuum domain. The CNT volume fraction is 3.49%. It should be noted that the bridging domains have regular block shapes so that the scaling parameters are linearly between 0 and 1 in the bridging domains.

In the multiscale model, an initial edge crack exists in the nanocomposite with its tip in the molecular domain so that the crack propagation can be restricted in the molecular domain. We consider linearly distributed displacements, as shown in Fig. 9, which are prescribed on the top and bottom of the model so we can clearly investigate the crack propagation phenomena in nanocomposites. The stress is calculated via dividing the total nodal/atomic force on the top of the nanocomposite by the area of its cross section. The calculated average stress is referred to as the effective stress in this article. We also calculate average strain as the effective strain.

The stress-strain relation is obtained based on multiscale simulations, as shown in Fig. 10, and compared with the stress-strain curve of Al crystalline with the same size as the simulated nanocomposite. As a difference from the Al crystalline, which exhibits ductile material characteristics, the nanocomposite is a brittle material. In the Al crystalline, the crack starts to propagate at 3% ef-

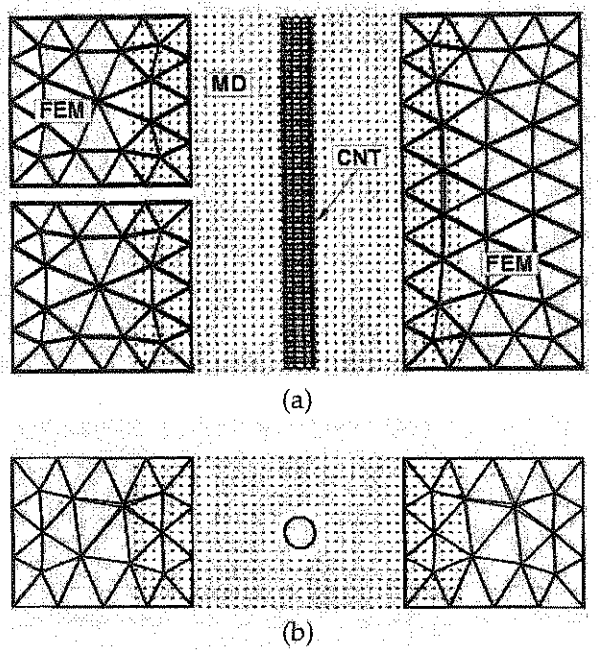

FIGURE 8. Multiscale model of nanocomposites containing (5,5) SWNTs for studying model I crack propagation: **a)** side view; **b)** top view

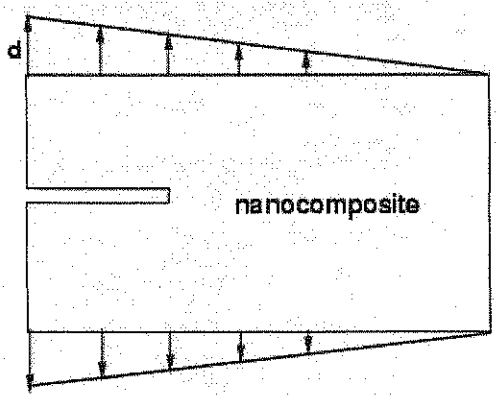

FIGURE 9. Scheme of the prescribed displacement on nanocomposites

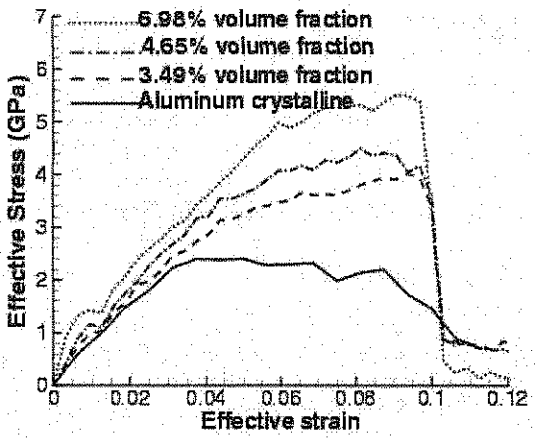

FIGURE 10. Stress-strain relations of nanocomposites reinforced with (5,5) SWNTs subject to fracture mode I compared with the stress-strain relation of Al crystalline

fective strain, until the aluminum fails around 10% effective strain. In the simulated nanocomposite, however, when the crack propagates and encounters the embedded SWNT, the nanotube bridges the crack, and the crack stops propagating. The nanocomposite fails when the embedded nanotube is broken. The above phenomena are illustrated in Fig. 11, which shows the configurations of the Al

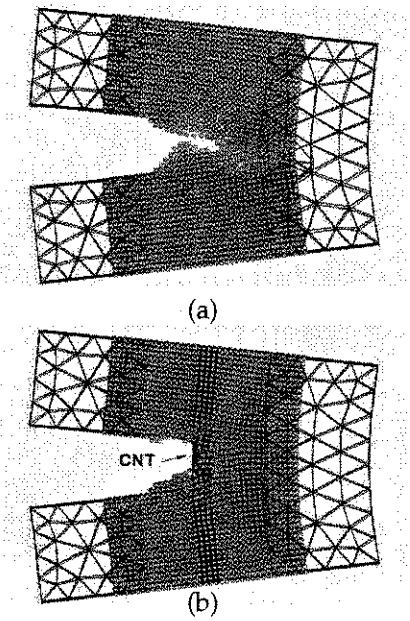

FIGURE 11. Configurations at 9% effective strain: a) aluminum crystalline; b) nanocomposite

crystalline and the nanocomposites at 9% effective strain. Consequently, the embedded nanotube enhances the strength of nanocomposites, i.e., the failure effective stress of 4.0 GPa compared with the failure effective stress of 2.4 GPa for Al crystalline.

We also vary the thickness and the length of the nanocomposite model in Fig. 8 to study fracture behavior of nanocomposites embedded with (5,5) SWNTs at different volume fractions. The stress-strain relations illustrated in Fig. 10 indicate that the failure effective stress is higher when CNTs with a larger volume fraction are embedded.

We then investigate fracture of nanocomposites embedded with various nanotubes: (21,21) SWNTs, (21,21) MWNTs, and (5,5) SWNT bundles, as studied in Section 4. The studied nanocomposites have the following dimensions: length 29.8 nm, width 5.6 nm, and height 8.1 nm. It should be noted that the Al crystalline with such a size could contain 95,514 Al atoms. The multiscale models for the simulated nanocomposites can be generated similarly to Fig. 8. In the continuum domain of the multiscale model, there are 2,295 finite element nodes and 9,679 tetrahedral elements. In the molecular domain, there are about 29,432 Al atoms and 4,116, 10,548, and 6,860 carbon atoms for a (21,21) SWNT, a (21,21) MWNT, and a (5,5) SWNT bundle, respectively. The volume fractions of nanotubes in all of the simulated nanocomposites are the same at 5.78%. Similar boundary conditions are applied to these composites, as indicated in Fig. 9. The temperature is maintained at 300 K. Fig. 12 compares

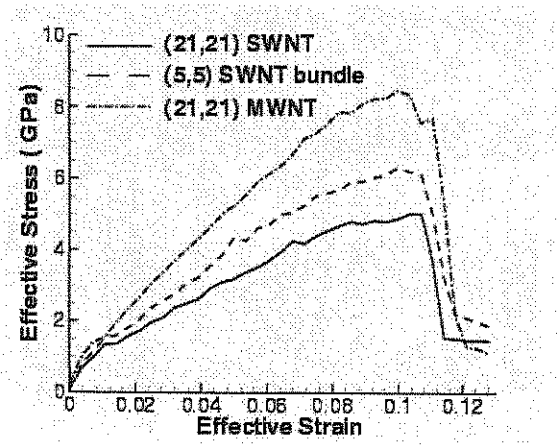

FIGURE 12. Stress-strain evolutions for fracture mode I of nanocomposites reinforced with (1) (21,21) SWNTs; (2) (21,21) MWNTs; and (3) (5,5) SWNT bundles

the stress-strain relations of nanocomposites subject to fracture mode I. It also illustrates the roles of the above three nanotube inclusions in resisting the crack propagation. It can be seen that the MWNT results in the most significant improvement to the composite strength, followed by the SWNT bundle. The SWNT results in the least significant improvement compared to the other two inclusions. Fig. 12 also shows that nanotube-reinforced composites are brittle materials. Once the tube is broken, the composites fail quickly.

6. CONCLUSIONS AND DISCUSSION

In this article, we first verified the bridging coupling method via studying the stress-strain relation of an aluminum crystalline bar and comparing it with molecular dynamics results. Then, this coupling method was employed to study Young's moduli of nanotube-based aluminum nanocomposites. SWNTs were considered as the inclusion first. Our numerical results showed that larger Young's moduli of nanocomposites could be achieved when a larger volume fraction of nanotubes was embedded. In addition, the size effect of SWNT on reinforcing nanocomposites was insignificant if the volume fractions of nanotubes were the same. We then investigated the role of three types of nanotubes in the reinforcement of nanocomposites: MWNTs, SWNT bundles, and SWNTs. We found that at the same volume fraction, the MWNT results in the most significant reinforcement, followed by the SWNT bundle. The SWNT results in the least significant reinforcement compared to the other two inclusions. We also studied the fracture of nanotube-based aluminum composites subject to fracture mode I. We found that when the crack tip encountered the embedded nanotube, the nanotube bridged the crack, and the crack propagation stopped. Therefore failure stresses of nanocomposites were increased compared with the failure stress of Al crystalline. Furthermore, a larger volume fraction of embedded SWNTs resulted in a larger failure stress of nanocomposites. Similar to their roles in the reinforcement of nanocomposites, MWNTs had the best ability to resist crack propagation, while SWNTs had the least ability when they were used as the inclusions with the same volume fraction.

In the literature, some examples of multiscale modeling of CNT-based nanocomposites treated the interfacial interaction via the continuum approach, such as micromechanics or the cohesive zone model, instead of direct MD simulation and were unable to thoroughly study the load transfer mechanism. An appropriate multiscale modeling of nanocomposites must include a molecular model for nanotubes and the interaction zones, including the CNT-matrix interface, and a continuum model for the rest of the matrix material. In this article, we demonstrated that the bridging domain coupling method could be an alternative solution. Although the studies in this article focused on nanotube-based aluminum composites, this coupling method can be extended to study other nanocomposites.

ACKNOWLEDGMENT

We acknowledge support from the Army Research Office (contract no. W911NF-06-C-0140).

REFERENCES

1. Iijima, S., Helical microtubules of graphitic carbon. *Nature* **354**:56–58, 1991.
2. Li, L. X., Li, F., Ying, Z., Yang, Q. H., and Cheng, H. M., Carbon nanotube/polymer functional composite. *New Carbon Mater.* **18**:69–74, 2003.
3. Xiao, S. P., Andersen, D. R., Han, R., and Hou, W. Y., Studies of carbon nanotube-based oscillators using molecular dynamics. *J. Comput. Theor. Nanosci.* **3**:143–147, 2006.
4. Zhao, Q. Z., Nardelli, M. B., and Bernholc, J., Ultimate strength of carbon nanotubes: A theoretical study. *Phys. Rev. B.* **65**:144105, 2002.
5. Berber, S., Kwon, Y. K., and Tomanek, D., Unusually high thermal conductivity of carbon nanotubes. *Phys. Rev. Lett.* **84**:4613–4616, 2000.
6. Dalton, A. B., Collins, S., Razal, J., Munoz, E., Ebron, V. H., Kim, B. G., Coleman, J. N., Ferraris, J. P., and Baughman, R. H., Continuous carbon nanotube composite fibers: Properties, potential applications, and problems. *J. Mater. Chem.* **14**:1–3, 2004.
7. Philip, B., Abraham, J. K., Chandrasekha, A., and Varadan, V. K., Carbon nanotube/PMMA composite thin films for gas-sensing applications. *Smart Mater. Struct.* **12**:935–939, 2003.

8. Fisher, F. T., Bradshaw, R. D., and Brinson, L. C., Fiber waviness in nanotube-reinforced polymer composites—I: Modulus predictions using effective nanotube properties. *Composites Sci. Technol.* **63**:1689–1703, 2003.
9. Rul, S., Lefevre-Schlick, F., Capria, E., Laurent, C., and Peigney, A., Percolation of single-walled carbon nanotubes in ceramic matrix nanocomposites. *Acta Mater.* **52**:1061–1067, 2004.
10. Hjortstam, O., Isberg, P., Soderholm, S., and Dai, H., Can we achieve ultra-low resistivity in carbon nanotube-based metal composites? *Appl. Phys. A* **78**:1175–1179, 2004.
11. Kuzumaki, T., Miyazawa, K., Ichinose, H., and Ito, K., Processing of carbon nanotube reinforced aluminum composite. *J. Mater. Res.* **13**:2445–2449, 1998.
12. Lordi, V., and Yao, N., Molecular mechanics of binding in carbon-nanotube-polymer composites. *J. Mater. Res.* **15**:2770–2779, 2000.
13. Velasco-Santos, C., Martinez-Hernandez, A. L., Lozada-Cassou, M., Alvarez-Castillo, A., and Castano, V. M., Chemical functionalization of carbon nanotubes through an organosilane. *Nanotechnology.* **13**:495–498, 2002.
14. Frankland, S. J. V., Harik, V. M., Odegard, G. M., Brenner, D. W., and Gates, T. S., The stress-strain behavior of polymer-nanotube composites from molecular dynamics simulation. *Composites Sci. Technol.* **63**:1655–1661, 2003.
15. Xiao, S. P., and Hou, W. Y., Fracture of vacancy-defected carbon nanotubes and their embedded nanocomposites. *Phys. Rev. B.* **73**:115406, 2006.
16. Tadmor, E. B., Phillips, R., and Ortiz, M., Hierarchical modeling in the mechanics of materials. *Int. J. Solids Struct.* **37**:379–389, 2000.
17. Xiao, S. P., and Yang, W. X., A nanoscale meshfree particle method with the implementation of the quasicontinuum method. *Int. J. Comput. Methods.* **2**:293–313, 2006.
18. Broughton, J., Abraham, F., Bernstein, N., and Kaxiras, E., Concurrent coupling of length scales: Methodology and application. *Phys. Rev. B.* **60**:2391–2403, 1999.
19. Curtin, W. A., and Miller, R. E., Atomistic/continuum coupling in computational materials science. *Model. Simul. Mater. Sci. Eng.* **11**:R33–R68, 2003.
20. Xiao, S. P., and Yang, W. X., Temperature-related Cauchy-Born rule for multiscale modeling of crystalline solids. *Comput. Mater. Sci.* **37**:374–379, 2006.
21. Xiao, S. P., and Yang, W. X., A temperature-related homogenization technique and its implementation in the meshfree particle method for nanoscale simulations. *Int. J. Numer. Methods Eng.* **69**:2099–2125, 2006.
22. Abraham, F., Broughton, J., Bernstein, N., and Kaxiras, E., Spanning the continuum to quantum length scales in a dynamic simulation of brittle fracture. *Europhys. Lett.* **44**:783–787, 1998.
23. Wagner, G. J., and Liu, W. K,. Coupling of atomistic and continuum simulations using a bridging scale decomposition. *J. Comput. Phys.* **190**:249–274, 2003.
24. Park, H. S., Karpov, E. G., Liu, W. K., and Klein, P. A., The bridging scale for two-dimensional atomistic/continuum coupling. *Philos. Mag.* **85**:79–113, 2005.
25. Belytschko, T., and Xiao, S. P., Coupling methods for continuum model with molecular model. *Int. J. Multiscale Comput. Eng.* **1**:115–126, 2003.
26. Xiao, S. P., and Belytschko, T., A bridging domain method for coupling continua with molecular dynamics. *Comput. Methods Appl. Mech. Eng.* **193**:1645–1669, 2004.
27. Guidault, P. A., and Belytschko, T., On the L2 and the H1 couplings for an overlapping domain decomposition method using Lagrange multipliers. *Int. J. Numer. Methods Eng.* **70**:322–350, 2007.
28. Xia, Z. H., and Curtin, W. A., Multiscale modeling of damage and failure in aluminum-matrix composites. *Composites Sci. Technol.* **61**:2247–2257, 2001.
29. Namilae, S., and Chandra, N., Multiscale model to study the effect of interfaces in carbon nanotube-based composites. *J. Eng. Mater. Technol.* **127**:222–232, 2005.
30. Belytschko, T., Liu, W. K., and Moran, B., *Nonlinear Finite Elements for Continua and Structures.*

John Wiley, New York, 2000.

31. Daw, M. S., and Baskes, M. I., Embedded-atom method: Derivation and application to impurities, surfaces, and other defects in metals. *Phys. Rev. B.* **29**:6443–6453, 1984.
32. Agrawal, P. M., Rice, B. M., and Thompson, D. L., Predicting trends in rate parameters for self-diffusion on FCC metal surfaces. *Surf. Sci.* **515**:21–35, 2002.
33. Hoover, W. G., Canonical dynamics—Equilibrium phase-space distributions. *Phys. Rev. A* **31**:1695–1697, 1985.
34. Belytschko, T., Xiao, S. P., Schatz, G. C., and Ruoff, R., Atomistic simulations for nanotube fracture. *Phys. Rev. B.* **65**:235430, 2002.
35. Xiao, S. P., and Hou, W. Y., Studies of size effects on carbon nanotubes' mechanical properties by using different potential functions. *Fullerenes Nanotubes Carbon Nanostructures.* **14**:9–16, 2006.
36. Yu, M. F., Lourie, O., Dyer, M. J., Moloni, K., Kelly, T. F., and Ruoff, R. S., Strength and breaking mechanism of multiwalled carbon nanotubes under tensile load. *Science.* **287**:637–640, 2000.
37. Girifalco, C. A., and Lad, R. A., Energy of cohesion, compressibility, and the potential energy functions of the graphite system. *J. Chem. Phys.* **25**:693–697, 1956.